Experimental study on bubble pairs and induced flow fields using tomographic particle image velocimetry

Hanbin Wang [1,2], Yang Xu [1,*], Jinjun Wang[1]

1: Fluid Mechanics Key Laboratory of Education Ministry, Beihang University, Beijing, 100191, China
2: Shenyuan Honors College, Beihang University, Beijing, 100191, China
* Correspondent author: xuyang@buaa.edu.cn

Keywords: Gas/liquid two-phase flow, Bubble motion, LIF-TPIV, Bubble-induced flow field.

ABSTRACT

Gas-liquid two-phase flows, such as bubbly flows, are widely used across various engineering and military applications due to their distinctive fluid dynamics. This study utilizes advanced imaging techniques, including shadowgraphy and laser-induced fluorescence tomographic particle image velocimetry (LIF-TPIV), to provide a quantitative analysis of bubble motions and the resulting flow fields. We systematically investigate the effects of orifice distances (s) set at 10, 15, 20, and 25 mm to assess the impact of spacing on bubble behavior and interactions. Our findings indicate that at orifice distances of 20 mm or less, the proximity of bubbles facilitates interactions, promoting dynamic bubble behaviors. In contrast, at distances greater than 25 mm, interactions become markedly weaker, leading to increased separation between bubbles during their free oscillation stages. This weak interaction directly influences the characteristics of bubble-induced flow fields. As orifice spacing increases, there is a noticeable decrease in the velocity of the flow field between bubbles, particularly noticeable at spacings of 20 mm and above. At these larger spacings, a low-velocity zone develops between the bubbles at higher heights, which, according to Bernoulli's principle, corresponds to a high-pressure area. This high pressure contributes to a reduction in bubble volume with increasing orifice spacing. Furthermore, the intensity of wake vortices between two bubbles is observed to be highest at the smallest spacing of 10 mm, closely resembling the flow structure characteristic of a single rising bubble. For spacings of 15 and 20 mm, the induced flow fields of the bubbles continue to interact significantly. However, at a spacing of 25 mm, the flow fields appear to function independently, suggesting a threshold beyond which bubble interactions stop to significantly affect their surrounding fluid environments. These findings are helpful for comprehending the two-phase flow dynamics, particularly in multi-orifices bubbly flow.

1. Introduction

Bubbly flows generated through liquid aeration, represent a two-phase system comprising a continuous liquid phase and a dispersed gas phase. These flows have significant impact on the mixing and transport characteristics of liquid, finding applications in diverse industrial fields,

including chemical and biological reactors, wastewater treatment, and nuclear plants (Hessenkemper & Ziegenhein (2018)). Choi et al. (2002) investigated the behavior of single bubbles and the distribution of flow fields in gas-liquid two-phase flows. Zhu et al. (2014) explored the dynamics of bubble formation, motion, and the development of bubbling characteristics such as bubble size, shape, and velocity. Bonnefis et al. (2023) highlighted that bubble instability is caused by the interaction between bubble and fluid motions, where flow disturbances influence bubble movement through pressure and viscous stress distributions on the bubble surface. These variations in bubble translation and rotation subsequently modify fluid dynamics via the boundary conditions at the bubble surface.

In addition to the study of single bubbles, research on multiple bubbles and even bubble pairs is also critically important. For instance, the effectiveness of engineering applications often relys on the behavioral characteristics of bubbles and the interactions between the continuous and dispersed phases (Ngoh & Lim (2016)). In the biological conversion of natural gas to liquid fuel, phenomena such as the coalescence of methane bubble pairs influence gas transfer within bacterial suspensions, impacting the overall biological conversion process of methane (Kim et al., 2016a). Therefore, exploring the dynamics of bubble pairs and the flow fields they induce holds significant practical importance. Talvy et al. (2000) posited that the movement characteristics of two bubbles are predominantly influenced by the leading bubble. Hallez & Legendre. (2011) investigated the interactions between two bubbles at medium Reynolds numbers, deriving a simple model based on physical parameters to calculate the drag and lift on each bubble. Zhang et al. (2021) explored the movement laws of a pair of rising bubbles through numerical simulation, discovering that the Eotvos number can determine the surface curvature of a bubble, which subsequently affects its trajectory.

Most two-phase flows exhibit turbulence and possess a highly three-dimensional, unsteady, and multi-scale nature (Takagi & Matsumoto (2011)). However, most current experimental research on bubble flows is primarily concentrated on two-dimensional plane measurements or relies on computational fluid dynamics (CFD). There exists an urgent need to develop three-dimensional measurement technology to fully capture the intricate three-dimensional information inherent in two-phase flows. This paper employed the laser-induced-fluorescence tomographic Particle Image Velocimetry (LIF-TPIV) method to examine the induced flow field of bubble pairs formed from submerged double orifices, with a specific emphasis on the effect of orifice distance. Additionally, the study explores the influence of the three-dimensional flow field structure on the bubble motion, aiming to contribute to a deeper understanding of the physical mechanism for the bubbly flow.

2. Experimental setup and method

2.1 Experimental setup

The experiment was conducted in a transparent Plexiglas tank measuring 600 mm × 600 mm × 600 mm, with a wall thickness of 20 mm as shown in Figure 1(a). The bubble generation setup consisted of two syringe pumps, two syringes, two ventilation tubes, and two orifices with an inner diameter (D_n) of 3 mm. Orifice distances (s) of 10, 15, 20, and 25 mm were selected to analyze the influence mechanism of orifice distance. The orifices were positioned at the bottom center of the tank, 70 mm from the bottom surface and approximately 520 mm from the free liquid surface, a height allowing bubbles to reach a steady state in the final stage of ascent (Wang et al. (2024)). Gas flow rate (GFR) was controlled by a high-precision medical syringe pump (LSP02-1B; Boading Longer Precision Pump Co. Ltd.), pushing a syringe with an inner diameter of 30 mm at a constant speed to achieve a GFR of $Q_g = 10$ ml/min.
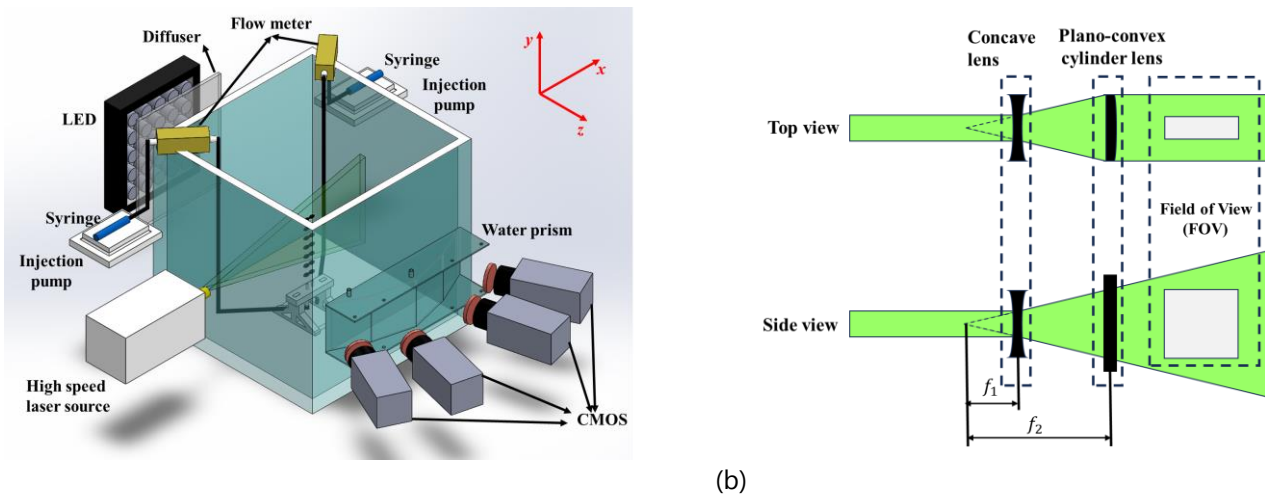

(a)
(b)

Figure 1. Experimental setup: (a) Time-resolved tomographic PIV; (b) Battery of lenses

Quantitative information about bubbles and their induced flow fields was obtained using a combination of shadowgraphy and LIF-TPIV. Illumination was provided by a Vlite-Hi-527–50 laser (Nd:YLF, 50 mJ per pulse at 1 kHz, from Beamtech Optronics Co., Ltd.), expanded by a battery of lenses shown in Figure 1 (b) to illuminate the measurement volume (60 × 60 × 20 mm³). This lens assembly included a concave lens with a focal length of $f_1 = 75$ mm and a plano-convex cylindrical lens with a focal length of $f_2 = 200$ mm. Four high-speed CMOS cameras (Photron Fastcam SA2/86K-M3) recorded images of bubble morphology and tracer particles. A water prism was placed between the camera and the water tank to reduce particle distortion. A high-pass filter with a cut-off wavelength of 560 nm was fitted in front of a Nikon lens (85 mm f/11D) to eliminate strong reflections from the laser at the gas–liquid interface and interference from ambient light sources. The CMOS camera had a resolution of 2048 × 2048 pixels, with a magnification of 0.045

mm/voxel. Fluorescent particles (PMMA Rhodamine B) with a nominal diameter of 7 μm served as PIV tracking particles, emitting fluorescence at 590 nm under 532 nm excitation.

2.2 Experimental method

In order to obtain quantitative information about the morphological properties and motion behavior of bubbles under cross-flow, the bubble identification method developed by Wang et al. (2024) was employed. The image noise reduction operation was omitted due to the lack of simultaneous measurements with the flow field. Edge recognition, image dilation, image filling, and image erosion operations were retained, as shown in Figure 2, and the bubble morphology obtained by this method closely matched the original images.
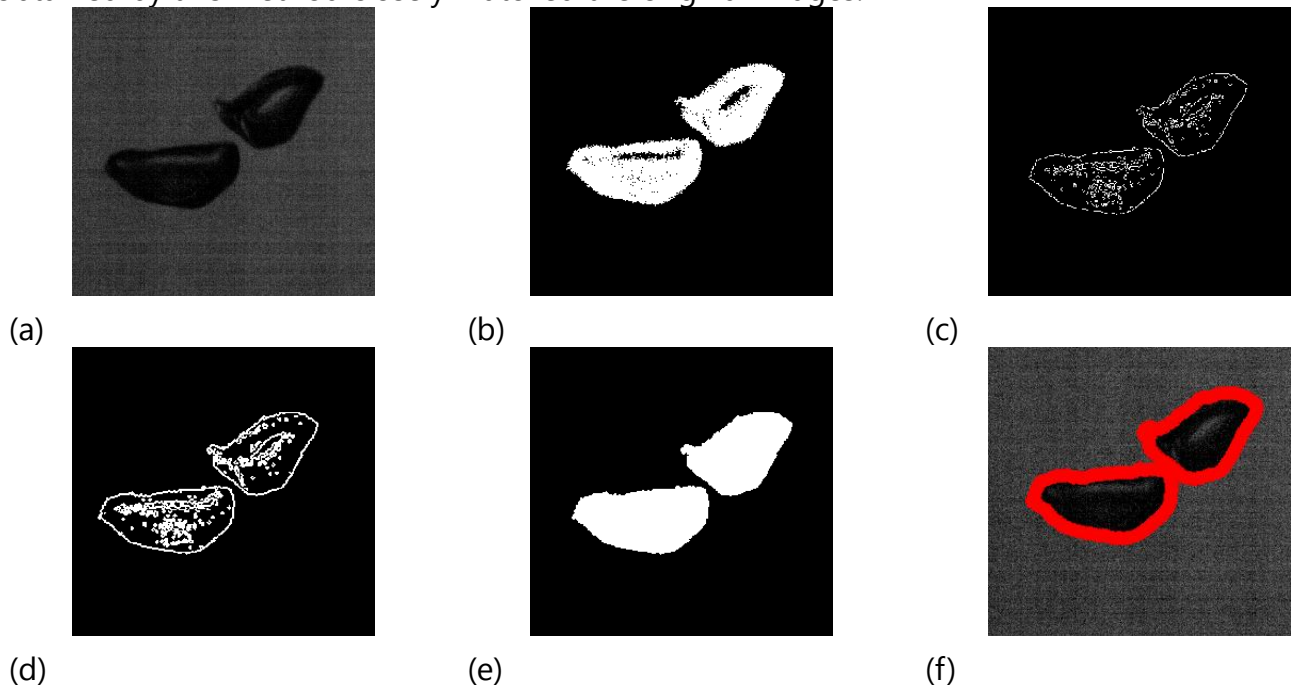

(a)   (b)   (c)

(d)   (e)   (f)

Figure 2. Bubble morphology recognition process: (a) Original image; (b) Edge recognition; (c) Image dilation; (d) Image filling; (e) Image erosion; (f) Comparison of bubble morphology with original image.

3. Result

3.1 Bubble shape

By using the bubble morphology recognition method as described above, it is possible to obtain quantitative information on the morphology of the bubbles, including their equivalent diameter and aspect ratio. Assuming an ellipsoidal bubble shape, the equivalent diameter d_b and aspect ratio χ of the bubble are calculated as follows (Kim et al., 2016b):

$$d_b = (d_l^2 d_s)^{1/3} \tag{1}$$

$$\chi = \frac{d_l}{d_s} \tag{2}$$

where d_l and d_s are the lengths of the long and short axes of the bubble, respectively. Figure 3 presents the Kernel Density Estimation (Parzen, 1962) for d_b and χ. With s ranging from 10-25 mm, the equivalent d_b progressively decrease from 5.52 mm to 4.92 mm, indicating that bubble volume decreases as the orifice spacing increases. The aspect ratio of the bubbles remains approximately constant at about 2 across all orifice spacings, suggesting a similar degree of deformation among the bubbles. The trend in equivalent diameter can be analysed using the Laplace-Young equation (Equation (3), de Gennes et al., 2004) to determine the pressure difference across the bubble interfaces. Assuming that the bubbles detach from the orifice with a consistent size and internal pressure across all conditions, and disregarding temperature variations during the rise, the Boyle-Marriott law equation (Equation (4)) is employed to assess the relationship between bubble volume and internal pressure. The resulting calculation is presented in Equation (5):

$$\Delta p = P_b - P = \frac{4\sigma}{d_b} \tag{3}$$

$$P_b V_b = P_{detach} V_{detach} \tag{4}$$

$$\frac{16}{3}\sigma d_b^2 + \frac{4}{3}\pi P d_b^3 = P_{detach} V_{detach} \tag{5}$$

where P is the pressure of fluid around the bubble, σ is the surface tension coefficient, P_b is the internal pressure of the bubble, P_{detach} is the internal pressure when the bubble detaches from the orifice, and V_{detach} is the volume of the bubble when the bubble detaches from the orifice. The above relationship indicates that bubble diameter is inversely proportional to environment pressure. As detailed in Section 3.2, with increasing orifice spacing, the velocity of the flow field between bubbles decreases. Particularly for spacings $s \geq 20$ mm, a low-velocity zone forms between the bubbles at higher elevations. According to Bernoulli's principle, this area is a high-pressure zone, leading to a reduction in bubble volume as the orifice spacing increases.
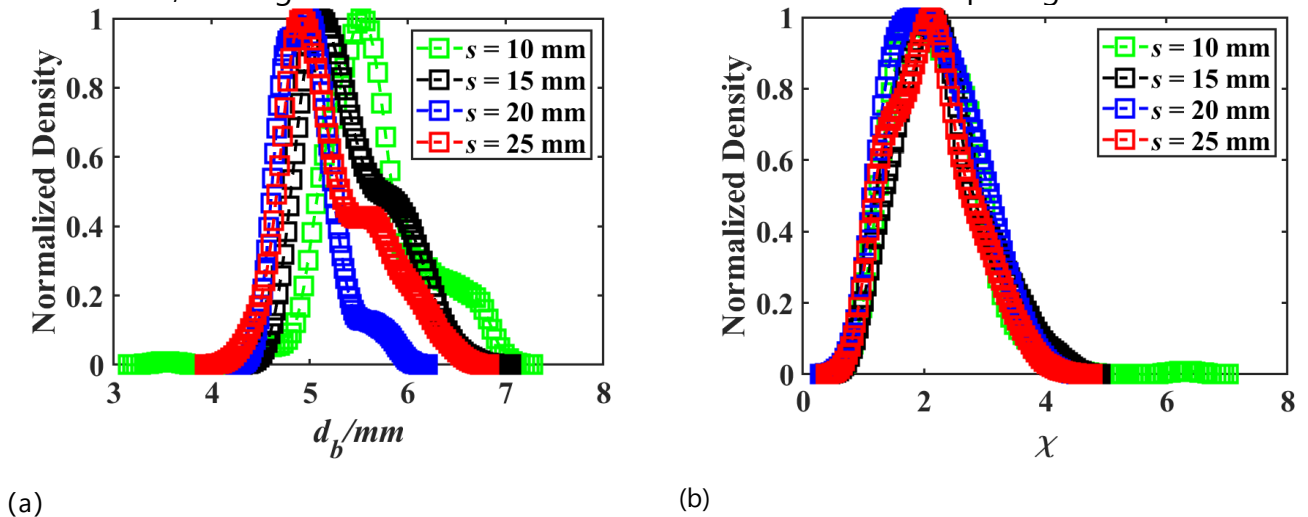

(a)   (b)

Figure 3. Kernel Density Estimation: (a) equivalent bubble diameter ($\boldsymbol{d_b}$); (b) bubble aspect ratio ($\boldsymbol{\chi}$).

3.2 Bubble motion

The rising trajectory of the bubbles is shown in Figure 4 (a). The results reveal a consistent pattern for each orifice distance, characterized by a rectilinear rise followed by oscillations. Regardless of orifice distance, the bubbles exhibit similar deflection directions and instability positions. The primary variable affecting the rising process of double-orifice bubbles is the bubble spacing (Δs), as shown in Figure 4(b). For s = 10, 15, and 20 mm, the Δs decreases during ascent, with the most significant reduction observed at s = 10 mm. Under this condition, the distance between bubbles reduce to approximately 55% of the orifice distance. In contrast, for s = 25 mm, Δs increases during rising, reaching a maximum of 130% of the orifice distance. The subsequent analysis will explore this phenomenon based on the obtained flow field results.
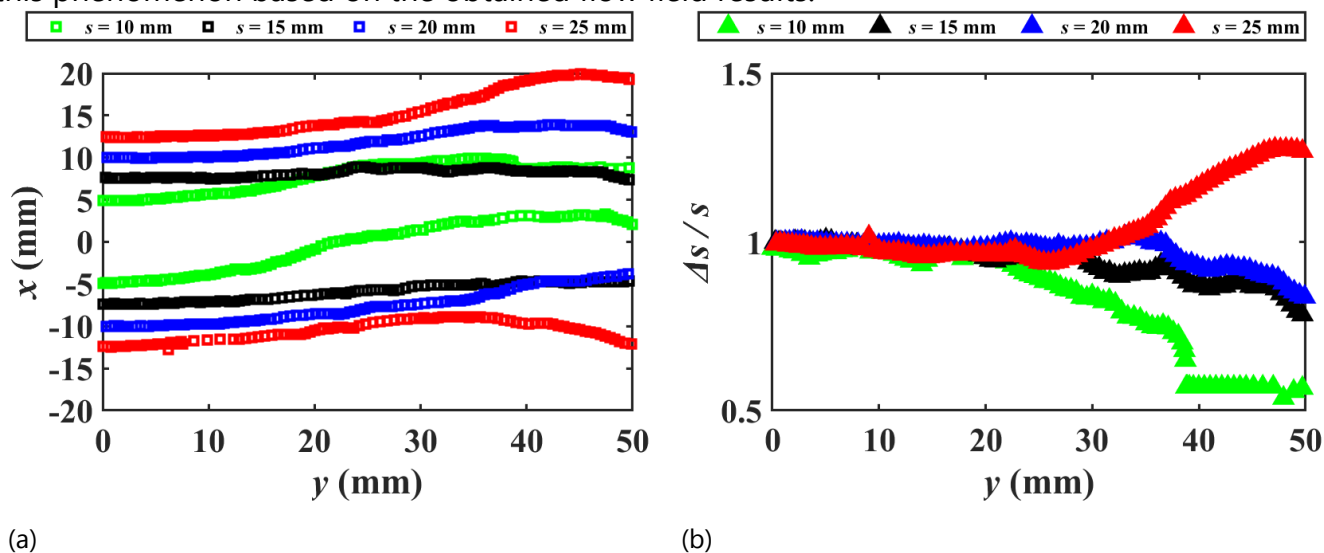

(a)

(b)

Figure 4. Bubble motion: (a) Bubble trajectory; (b) Bubble spacing

3.3 Time-averaged velocity distribution

Figure 5 shows the time-average profile of the axial velocity distribution in the $z = 0$ plane. For the $s = 10$ mm, the flow field exhibits two distinct peaks of normal distribution at $y \leq 30$ mm. Beyond $y \geq 40$ mm, a single velocity peak is observed, similar to the results of single-orifice bubbly-flow field from Wang et al (2024), suggesting a similarity to a single-bubble condition due to the close proximity of bubbles. For s = 15 and 20 mm, the bubble-induced flow field consistently displays two velocity peaks with a difference between them. This difference corresponds to the observed reduction in bubble spacing (Δs) shown in Figure 4, supporting the idea of interaction between bubbles. In the case of s = 25 mm, the bubble-induced flow field maintains two

approximately equal-sized peaks, signalling minimal interaction between bubbles. This agrees with the slight increase in *Δs* observed during the free oscillation stage in Figure 4.
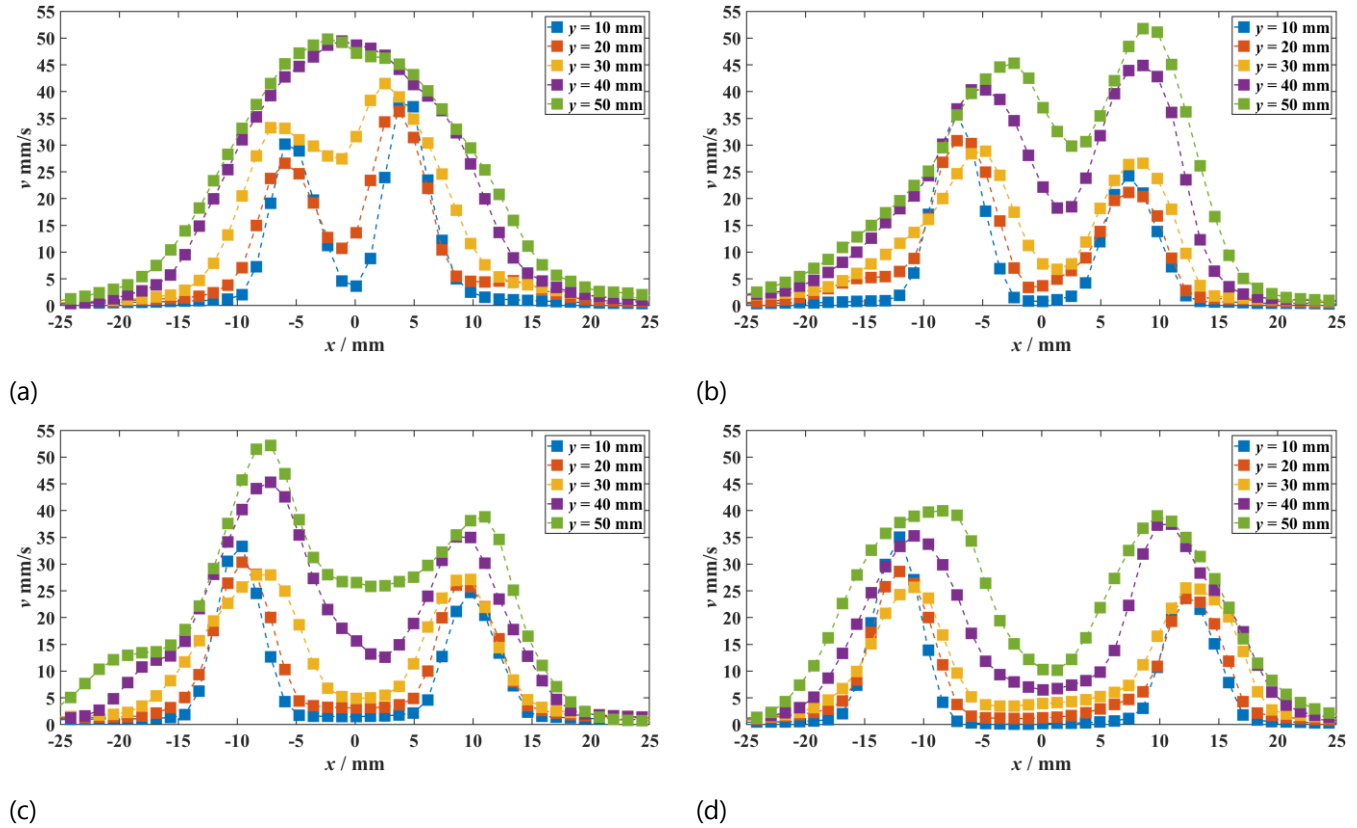

Figure 5. Time-averaged axial velocity distribution: (a) $s = 10$ mm; (b) $s = 15$ mm; (c) $s = 20$ mm; (d) $s = 25$ mm.

3.4 Evolution of instantaneous flow field

Figure 6 shows the three-dimensional vorticity field of the bubble-induced flow field, and the observations agree with the time-averaged flow field in Sec 3.3. At $s = 10$ mm, the bubble generates two distinct vortex rings near the orifice. Interaction occurs between the vortex rings around $y = 30$ mm, and by $y = 40$ mm, the vortex rings merge into a filament structure resembling that of a single bubble as described in She et al (2021). For $s = 15$ and 20 mm, the two bubbles create independent vortex rings near the orifice. with each bubble forms the second wake vortex ring around $y = 30$ mm. Beyond $y = 40$ mm, the second vortex rings shed. The three-dimensional vortex structure diagram clearly shows a spatial overlap area between the vortex structures of the two bubble, indicating interaction between the bubble-induced flow fields. For $s = 25$ mm, the wake vortex structures induced by the two bubbles are spatially distant and do not interact. This spatial separation agrees with the axial velocity distribution observed in Figure 5.
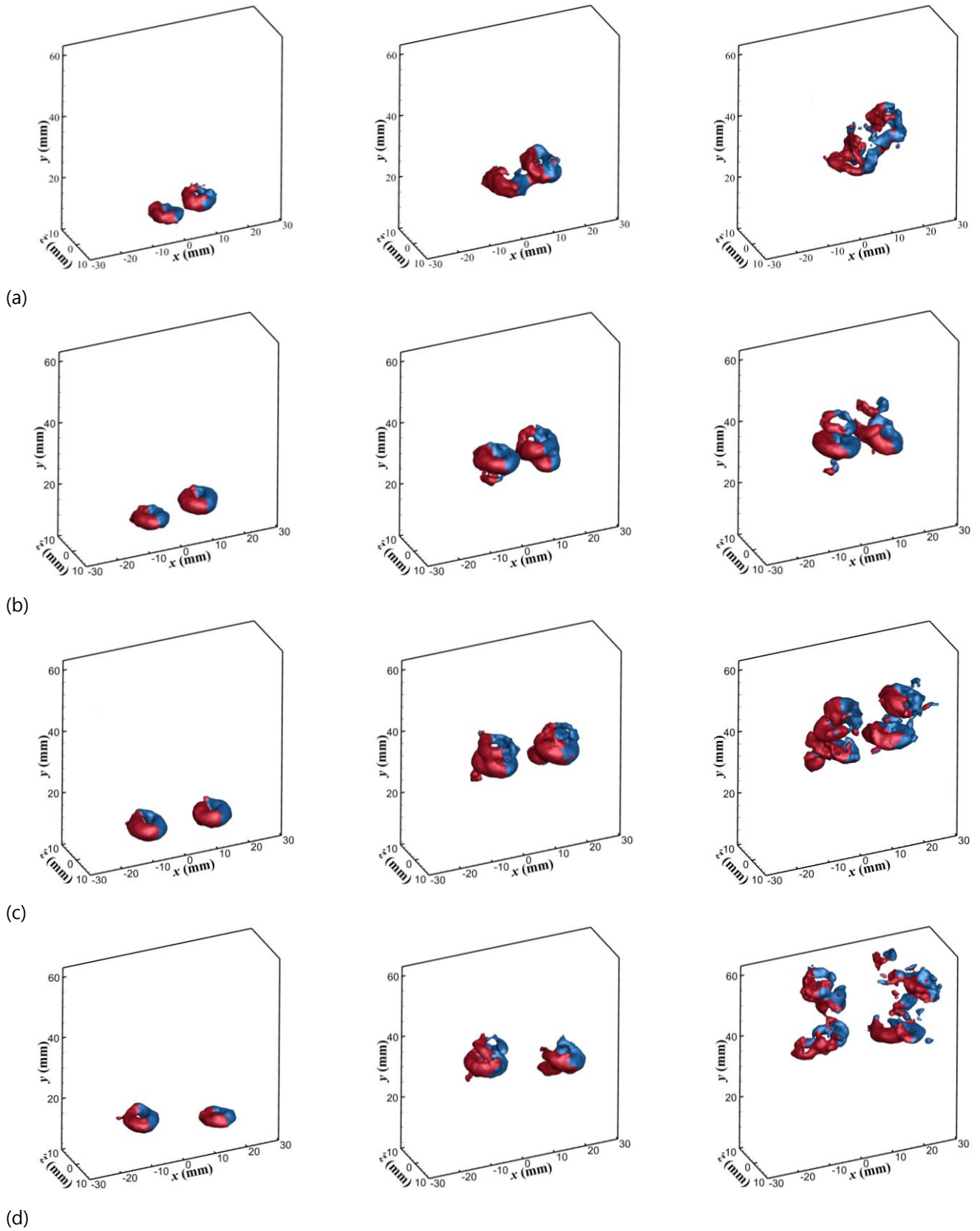
(a)

(b)

(c)

(d)

Figure 6 Time evolution of three-dimensional bubble-induced vortex field: (a) $s = 10$ mm; (b) $s = 15$ mm; (c) $s = 20$ mm; (d) $s = 25$ mm.

4. Conclusions

This study employed shadowgraphy and LIF-TPIV to investigate bubbles and their induced flow fields, focusing on analyzing the impact of orifice distance. The main conclusions are as follows: in terms of bubble motion, when $s \leq 20$ mm, the Δs remains constant initially and gradually decreases during rising. Conversely, when the $s > 25$ mm, the Δs gradually increases during rising. Regarding the bubble-induced flow field, a noticeable decrease in the velocity of the flow field between bubbles is observed as $s = 20$ mm and above. According to Bernoulli's principle, this low-velocity zone correlates with a high-pressure area. This increased pressure significantly contributes to a reduction in bubble volume as the orifice spacing widens. For $s = 10$ mm, the interaction between the flow fields induced by two bubbles is strongest. The vortex structures between the two bubbles merge, resembling the pattern of a single bubble. For $s = 15$ and 20 mm, the induced vortex structures by two bubbles still exhibit interaction. For $s = 25$ mm, the wake structure formed by the two bubbles are independent.

References

Bonnefis, P., Fabre, D., & Magnaudet, J. (2023). When, how, and why the path of an air bubble rising in pure water becomes unstable. *Proceedings of the National Academy of Sciences*, 120(11), e2300897120.

Choi, H. M., Terauchi, T., Monji, H., & Matsui, G. (2002). Visualization of Bubble-Fluid Interaction by a Moving Object Flow Image Analyzer System. *Annals of the New York Academy of Sciences*, 972(1), 235-241.

de Gennes, P.-G., Brochard-Wyart, F., & Quéré, D. (2004). Capillarity and Wetting Phenomena. *In Capillarity and Wetting Phenomena*. Springer New York.

Hallez, Y., & Legendre, D. (2011). Interaction between two spherical bubbles rising in a viscous liquid. *Journal of Fluid Mechanics*, 673, 406-431.

Hessenkemper, H., & Ziegenhein, T. (2018). Particle shadow velocimetry (PSV) in bubbly flows. *International Journal of Multiphase Flow*, 106, 268-279.

Kim, K., Lee, J., Seo, K., Kim, M. G., Ha, K. S., & Kim, C. (2016). Enhancement of methane–water volumetric mass transfer coefficient by inhibiting bubble coalescence with electrolyte. *Journal of Industrial and Engineering Chemistry*, 33, 326-329.

Kim, M., Lee, J. H., & Park, H. (2016). Study of bubble-induced turbulence in upward laminar bubbly pipe flows measured with a two-phase particle image velocimetry. *Experiments in Fluids*, 57, 1-21.

Ngoh, J., & Lim, E. W. C. (2016). Effects of particle size and bubbling behavior on heat transfer in gas fluidized beds. *Applied Thermal Engineering*, 105, 225-242.

Parzen, E. (1962). On Estimation of a Probability Density Function and Mode. *The Annals of Mathematical Statistics*. 33 (3): 1065–1076.

She, W. X., Gao, Q., Zuo, Z. Y., Liao, X. W., Zhao, L., Zhang, L. X., & Shao, X. M. (2021). Experimental study on a zigzagging bubble using tomographic particle image velocimetry with shadow image reconstruction. *Physics of Fluids*, 33(8).

Takagi, S., & Matsumoto, Y. (2011). Surfactant effects on bubble motion and bubbly flows. *Annual Review of Fluid Mechanics*, 43, 615-636.

Talvy, C. A., Shemer, L., & Barnea, D. (2000). On the interaction between two consecutive elongated bubbles in a vertical pipe. *International Journal of Multiphase Flow*, 26(12), 1905-1923.

Wang, H. B., Xu, Y., Li, S. Y., & Wang, J. J. (2024). Effects of gas flow rate on rising bubble chains and induced flow fields: An experimental study. *International Journal of Multiphase Flow*, 170, 104623.

Zhang, J., Ni, M. J., & Magnaudet, J. (2021). Three-dimensional dynamics of a pair of deformable bubbles rising initially in line. Part 1. *Moderately inertial regimes. Journal of Fluid Mechanics*, 920, A16.

Zhu, X., Xie, J., Liao, Q., Chen, R., & Wang, H. (2014). Dynamic bubbling behaviors on a micro-orifice submerged in stagnant liquid. *International Journal of Heat and Mass Transfer*, 68, 324-331.